

Study of the Dynamics of Large Reflector Antennas with Accelerometers

Ralph C. Snel, Jeffrey G. Mangum, and Jacob W. M. Baars

Abstract—The Atacama Large Millimeter Array (ALMA) will consist of up to 64 state-of-the-art sub-mm telescopes, subject to stringent performance specifications which will push the boundaries of the technology, and makes testing of antenna performance a likewise challenging task. Two antenna prototypes were evaluated at the ALMA Test Facility at the Very Large Array site in New Mexico, USA. The dynamic behaviour of the antennas under operational conditions was investigated with the help of an accelerometer system capable of measuring rigid body motion of the elevation structure of the antenna, as well as a few low-order deformation modes, resulting in dynamic performance numbers for pointing stability, reflector surface stability, path length stability, and structure flexure. Special emphasis was given to wind effects, one of the major factors affecting performance on timescales of seconds to tens of minutes.

Though the accelerometers could not directly measure antenna performance on timescales longer than 10 seconds, it was possible to use them to derive antenna properties which allowed extrapolation of the wind-affected performance to timescales of 15 minutes and longer. This paper describes the accelerometer system, its capabilities and limitations, and presents the dynamic performance results of the two prototype antennas investigated.

In addition to verification of the performance requirements, we investigated the vibration environment on the antennas, relevant for vibration-sensitive equipment for use on the ALMA antennas, the lowest eigenfrequencies for the antennas, and the sensitivity to vibration generated by similar antennas operating nearby.

This work shows that seismic accelerometers can successfully be used for characterisation of antenna dynamics, in particular when complemented with simultaneous wind measurements and measurements for static performance. The versatility of the accelerometers also makes them a valuable tool for troubleshooting of unforeseen antenna features.

Index Terms—ALMA, Antenna measurements, Acceleration measurement, Dynamic response Dynamics, Millimeter wave antennas, Radio telescope, Wind

I. INTRODUCTION

The enormous growth of radio astronomy in the millimeter and submillimeter wavelength regime (frequencies from 100 - 1000 GHz) over the last 25 years has been made possible both by the emergence of sensitive detectors like SIS-diodes and HEB-devices and the construction of ever larger and more accurate radio telescopes. Reflector antennas for this wavelength region have been built from relatively small (up to 15 m diameter), extremely accurate (reflector accuracy 15 - 25 μm) submillimeter telescopes to larger (20 - 45 m) millimeter antennas with surface accuracy from 75 - 150 μm .

Manuscript received July 10, 2006; revised November 30, 2006.

The performance results presented in this publication were part of a comprehensive technical evaluation process used to evaluate the ALMA prototype antennas which concluded in April 2005.

Current projects in this area are the 50 m diameter Large Millimeter Telescope (LMT) under construction in Mexico [1], which is aiming to reach 75 μm rms surface and 1 arcsec pointing accuracy and the Atacama Large Millimeter Array (ALMA). ALMA is a global collaboration of North America (USA and Canada) and Europe (European Southern Observatory) with contributions from Japan to build a powerful millimeter wavelength aperture synthesis array at a 5000 m high plateau in Northern Chile. The instrument will consist of up to 64 high accuracy Cassegrain reflector antennas of 12 m diameter with a surface rms accuracy of 20 μm and a pointing and tracking accuracy and stability of 0.6 arcseconds, all under the severe operational conditions of the high site. This telescope will operate over the entire frequency range from 30 to 950 GHz.

These specifications are among the most severe ever realised in radio telescopes and force the designer and manufacturer to push the boundaries of the technology. At the same time, it is becoming increasingly difficult for the contractor and the customer to quantitatively and reliably evaluate the performance characteristics of these instruments. At the longer wavelengths radio astronomers have developed and used methods of antenna evaluation which are based on the use of strong cosmic radio sources and astronomical observing techniques [2]. These measurements are only of limited use at the short millimeter wavelengths at frequencies above 100 GHz. The number of suitable cosmic test sources is severely limited because of their intrinsic weakness and the sensitivity limitations of the relatively small antennas.

For the ALMA Project the partners decided early to obtain two prototype antennas from different design and fabrication groups to increase the chance of achieving the desired performance. The prototype antennas tested here, one designed and constructed by VertexRSI, the other by a consortium of Alcatel and European Industrial Engineering, hereafter referred to as AEC, are similar in overall design and built to meet identical requirements, though significant differences exist in the approaches taken to meet these requirements. The antennas, together with a third one from Japan, are located at the ALMA Test Facility (ATF), on the site of the Very Large Array (VLA) in New Mexico, USA (Figures 1 and 2). For more information on the antennas and the evaluation program, see [3].

An international team of radio astronomers was formed to subject the antennas to an extensive evaluation program. In preparing their tasks this group determined that additional measurements and test methods and instruments beyond the



Fig. 1. The VertexRSI ALMA prototype antenna.



Fig. 2. The ALMA Test Facility, with the AEC antenna (left), VertexRSI antenna (middle) and Mitsubishi antenna (right).

usual astronomical testing would be needed to check the very stringent specification of the antennas. A particularly important, but difficult to measure quantity is the accuracy with which the antenna can be pointed at arbitrary positions on the sky and the stability with which such a pointing can be maintained under the influence of variations in temperature and wind forces. Given our need to check these parameters independently of the availability of celestial radio sources, we looked into the possibility of using accelerometers on the antenna structure to establish its dynamical behaviour.

The use of seismic accelerometers for performance characterization has been successfully demonstrated on optical telescopes [4] and mm-antennas [5], [6]. Using a set of 10 seismic accelerometers, installed on the antenna back-up structure (BUS), subreflector support structure (apex), and receiver cabin, we have measured accelerations allowing determination of rigid body motion of the elevation structure, and a few low-order distortions of the BUS.

The nature of the accelerometers used in this work limits accurate displacement measurement to time scales of at most 10 seconds or frequencies of at least 0.1 Hz. Since this is well below the lowest eigenfrequencies of the antennas, this is sufficient to determine dynamic antenna behaviour. For the frequency range covered accurately by the accelerometers, approximately 0.1 to 30 Hz, it is possible to check the following antenna specifications:

- 1) Variations in surface shape, restricted to large scale effects like focal length and astigmatism
- 2) Variations in pointing in elevation and cross-elevation direction
- 3) Translation of apex structure with respect to the BUS
- 4) Variations in path length along the boresight direction

Using detailed long term wind studies, and wind measurements simultaneous with accelerometer measurements, antenna performance can be extrapolated to longer time scales under the assumption that wind effects dominate antenna performance on these time scales.

Antenna performance should be met for all modes in which the antenna will be used to perform astronomical observations. For this paper, we have considered

- 1) pointing where the antenna is commanded to remain fixed at an azimuth and elevation position,
- 2) sidereal tracking, where azimuth and elevation are updated continuously,
- 3) fast switching mode, where the antenna is switched quickly between two neighbouring points,
- 4) interferometric mosaicking, in which areas of sky are mapped at slow speed (0.05 deg/s),
- 5) on-the-fly mapping (OTF), in which large areas of sky are mapped at high scan speed (0.5 deg/s).

II. ACCELEROMETER SETUP

We placed 10 accelerometers on the antenna in the following configuration (Figure 3):

- 3 accelerometers as a 3-axis sensor on the subreflector structure (A1,2,3)

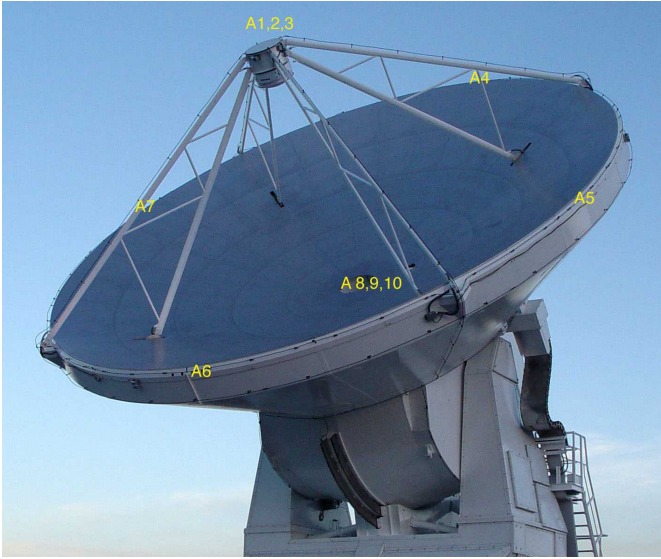


Fig. 3. Placement of the accelerometers on the antenna.

- 4 accelerometers along the rim of the BUS in boresight direction (A4-A7)
- 3 accelerometers as a 3-axis sensor on the receiver flange invar ring (A8,9,10)

The accelerometers used for the tests are Endevco model 86 seismic accelerometers. Together with a multichannel 24 bit A/D converter, the noise properties are as shown in Figure 4, red curve. The noise spectrum in acceleration is somewhat constant with frequency in the range 0.1 - 10 Hz, but since the accelerometers will be used to measure displacement, the acceleration needs to be integrated twice. This turns the originally white noise into “red” noise, with high power at low frequencies. In Figure 4, the green curve shows the RMS displacement noise as a function of frequency, where the integration has been applied. For frequencies above a few Hz, measurement accuracy is better than 10 nm, while at 0.1 Hz accuracy has deteriorated to just below half a μm . The accelerometers were read out at a frequency of 100 Hz. Accelerometer resonance occurs around 200 - 300 Hz, which required a hardware anti-alias filter which cuts in above 10 Hz. Effectively this allows antenna vibrations up to about 30 Hz to be measured.

On the low frequency side, both the accelerometers and the read-out electronics cut off frequencies below approximately 0.007 Hz. Note that the DC or static component can not be measured, which implies that only position or offset pointing changes can be detected. For most practical purposes encountered during antenna testing, antenna vibrations below 0.1 to 0.3 Hz are affected by noise. Within the frequency range 0.1 Hz to 30 Hz the sensitivity for displacements is better than a few micrometers, or sub-arcsecond for pointing.

The measurements are time series of accelerations or properties derived from this. In most cases, this is not particularly informative, partly because of the limited frequency bandwidth of the signal. Therefore the choice was made to present most results in the form of power spectra. Integration of the signal corresponds to division by the frequency of the power

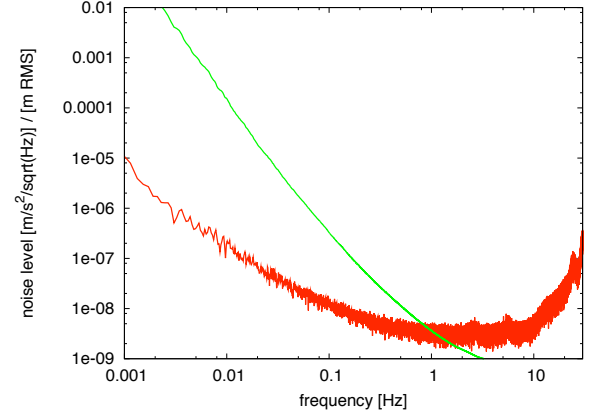


Fig. 4. Accelerometer and read-out equipment noise. The red curve is the spectral noise in $\text{m/s}^2/\sqrt{\text{Hz}}$, the green curve is the RMS noise in meters. The value at frequency ν Hz shows the typical RMS noise over timescales of $\frac{1}{\nu}$ seconds.

spectrum, and RMS deviations from the average time series is simply integration over the power spectrum. In order to reduce noise in the power spectrum, we can sacrifice low frequency range and frequency resolution by averaging the power spectra of a number of shorter time series instead of one long series. Using this noise reduction, reproducible features show up more clearly in the power spectra.

The normalisation for the power spectrum used in this work is with the square of the length n of the time series, and values at negative frequencies are added to those at positive ones:

$$\hat{A}(\nu) = \frac{|FFT(A(t))|^2}{n^2} \quad (1)$$

with $A(t)$ a time series with n samples as a function of time, FFT the fast Fourier transform, and ν the frequency. Note that in the plots in this paper $\sqrt{\hat{A}(\nu)}$ is plotted. The units along the ordinate reflect this.

RMS stability of a measured parameter is presented as a function of frequency:

$$RMS(\nu) = \sqrt{\sum_{\nu'=\nu}^{\infty} \hat{A}(\nu')} \quad (2)$$

This type of presentation has the property that at zero frequency, the RMS is that of $A(t)$, while at higher frequencies the RMS decreases to include only those contributions from frequencies above and including ν . An oscillation at a given frequency shows up as a jump in the RMS curve at this frequency. In addition to accelerometer and amplifier noise, thermal effects on the accelerometers and small tilt variations of the accelerometers in the gravity field, add additional low frequency noise to the measurements.

In order to obtain pointing and displacement data from the accelerations, the location and orientation of the accelerometers need to be known. This was determined from known and large antenna motions, imposed through the drive system.

Through combination of selected accelerometer signals, the following antenna motions could be isolated:

- Elevation pointing (top and bottom accelerometers on the rim of the BUS)
- Cross-elevation pointing (left and right accelerometers on the rim of the BUS)
- Boresight motion of BUS (4 accelerometers on the rim of the BUS, one on receiver flange)
- Path length stability (boresight motion of BUS plus accelerometer on apex structure)
- “Focal length” stability or “defocus” or “apex axial motion” of BUS (4 accelerometers on the rim of the BUS, one on receiver flange)
- “+” astigmatism of BUS (4 accelerometers on the rim of the BUS)

The accelerometers on the BUS are configured to measure deformations which can be described with low order Zernike polynomials [7]. Path length changes, caused by motion of the entire BUS as a rigid body along the boresight direction, can be described as the $(n=0, m=0)$ Z_0^0 “piston” term; changes in elevation pointing as the $(n=1, m=1)$ Z_1^1 “tilt” term; changes in cross-elevation pointing as the $(n=1, m=-1)$ Z_1^{-1} “tip” term; boresight motion of the rim of the BUS with respect to the receiver flange, considered to be representative for the vertex of the antenna, as the $(n=2, m=0)$ Z_2^0 “defocus” term; boresight deformation of the left and right side of the rim of the BUS in opposite direction as the top and bottom side of the BUS, as the $(n=2, m=2)$ Z_2^2 “+ - astigmatism” term. Due to the limited number of accelerometers on the rim of the BUS, the $(n=2, m=-2)$ Z_2^{-2} “× - astigmatism” term can not be measured.

III. TEST CONDITIONS

Environmental conditions have a significant influence on the performance of the antenna. On the time scales relevant for the accelerometer measurements, the major environmental effects are caused by the wind. To draw meaningful conclusions from the measurements, it was thus necessary to carefully characterise the local wind through wind measurements both independent of as well as simultaneous with the accelerometer measurements.

In addition to variable wind conditions, the thermal environment affects antenna performance. Since thermal effects of the antenna are on timescales longer than those accurately measurable with the accelerometers, they will not be considered for the measurements presented here [8].

A. Wind Conditions

Wind data at the ATF were recorded over a period of more than a year, sampled continuously at 10 Hz with a sonic anemometer, placed some 30 m north of the antennas. The power spectrum of the wind speed over intervals of approximately 1000 seconds was determined as a function of average wind speed and direction.

The local terrain and building geometry affect the wind power spectrum. Overall, the terrain is reasonably flat out to more than 10 km in any direction. Seen from the anemometer, the VLA control building is located a few hundred meters

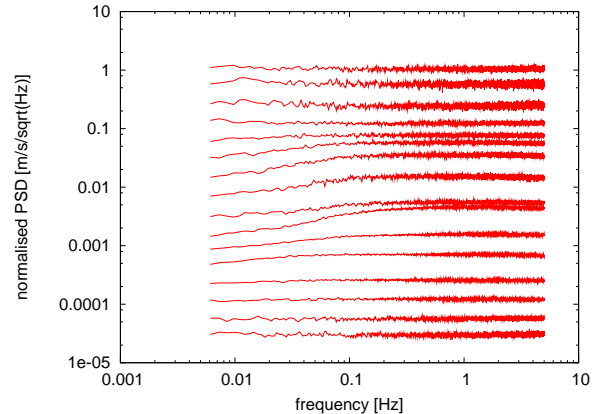


Fig. 5. Wind power spectra, normalised with the typical undisturbed wind spectrum. The 16 curves show equally spaced wind directions, centered on the sonic anemometer, starting at north (top) and increasing clockwise. Each subsequent spectrum is shifted by a factor 0.5 for clarity. Only wind speeds over 2.5 m/s were used.

towards the west, the Mitsubishi prototype antenna about 30 m to the south-west, the VertexRSI prototype antenna about 30 m to the south-south-east, and the AEC prototype antenna about 50 m to the south-east.

The wind power spectrum has a typical slope of $\nu^{-1.5}$, where ν is the frequency. From theory, an exponent of $-\frac{5}{3}$ is expected for the microscale range, while an exponent of -1 is expected for the mesoscale turbulence range. The measured exponent is consistent with theory, showing a transition between micro- and mesoscale turbulence.

The effect of obstructions on the power spectrum seems to increase the high frequency power in the spectrum, while keeping the same exponent. In addition, the low frequency part is lowered and the exponent is decreased towards lower frequencies. The observed transition between low and high frequency is around 0.1 Hz.

Figure 5 shows the wind power spectra, normalised with the typical undisturbed wind spectrum, for 16 equally spaced wind directions, starting at the north and stepping through the east. Only wind speeds over 2.5 m/s were used.

Figure 6 shows the normalised power spectra of Figure 5 averaged over the frequency range between 0.3 and 2.0 Hz, plotted as a function of azimuth. The shape of the curve can easily be explained by the positions of the antennas and the VLA control building.

The wind power spectra show distinct features depending on the wind direction. The sonic anemometer can clearly distinguish the VLA control building, Mitsubishi antenna, the clearance between the Mitsubishi and VertexRSI antennas, and the combined effect of the VertexRSI and AEC antennas. This directional dependence complicates interpretation of the wind results. Because any obstruction will be at different azimuths for the antenna and the sonic anemometer, they will be subjected to a different wind spectrum.

Three of the four peaks in Figure 6 show the wake turbu-

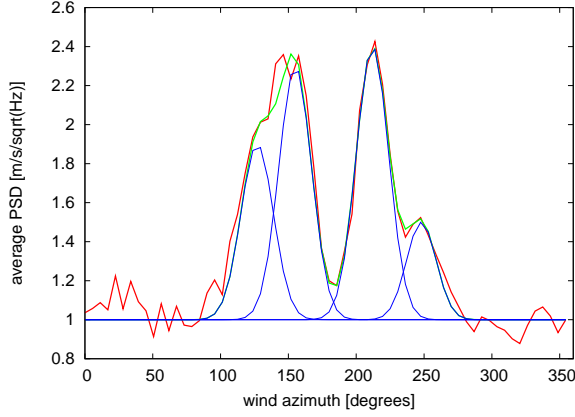


Fig. 6. Normalised wind power spectra averaged over 0.3 - 2.0 Hz, as a function of wind direction, as seen from the sonic anemometer. The peak between 90 and 180 degrees is the combined effect of the AEC and VertexRSI antenna, the peak between 180 and 240 is due to the Mitsubishi antenna, and the peak around 250 degrees is due to the VLA control building. The red curve shows the measured turbulence component, while the green curve shows an analytical approximation composed of 4 gaussian components matched to the observed peaks. The 4 individual components are shown as blue lines.

lence of an antenna. This information is used to correct the wind spectra as experienced by the antennas in order to predict performance for undisturbed wind conditions, but can also be used to predict performance for an antenna in the compact configuration of the ALMA array, where the antennas are only a few tens of meters apart.

The wind power spectra are needed to scale the antenna vibration power spectra to that for a reference wind spectrum. Since for short (typically 15 minutes) measurements the error bars on a single power spectrum can be large, and the natural variations in the wind can throw off an observed power spectrum far away from the average, the following wind spectral features were used to treat wind effects.

- 1) Effects of upwind obstructions change the shape of the power spectrum, but above frequencies of approximately 0.2 Hz the result is effectively a change in the level of the power spectrum, while the slope remains unchanged and close to the theoretically expected value (Figure 5).
- 2) For frequencies above approximately 1 Hz, effects of aliasing become visible, introducing errors in the measured slope.

These effects combined leave a frequency interval between 0.2 and 1.0 Hz where the slope of the power spectrum is reasonably well-defined, and independent of upwind obstructions. This interval is used for normalisation of the power spectra, instead of the average wind speed, which may be affected by obstructions and stochastic effects.

Prediction of low frequency wind effects was done using the average power spectra calculated from all available wind data, and extrapolation from the 0.2 - 1.0 Hz range. Known obstructions (Figure 6, and a modification of it to reflect the obstructions as seen by the antennas) and variation of the power spectra with wind speed were taken into account.

B. Wind Scaling

The dynamic wind pressure on the structure is a function of frequency. For a single point, the pressure can be directly coupled to the power spectrum of the square of the wind speed. For extended structures spatial averaging will occur. Thus, for turbulence of a geometric scale smaller than the typical dimension of the structure, the effective pressure is less than for turbulence of larger scale, given the same power spectral density: the antenna serves as a mechanical low-pass filter. The averaging effect of the dynamic wind pressure can be described with the aerodynamic admittance function (AAF) of the form

$$AAF(\nu) = \frac{1}{1 + \left(2\nu \frac{L}{U}\right)^{\frac{4}{3}}} \quad (3)$$

where L is the typical scale of the structure, and U is the average wind speed [9]. Since the average wind speed varies from measurement to measurement, the AAF also varies.

The (static) wind force on a structure is given by

$$F_{wind} = \frac{1}{2} \cdot C_d \cdot L^2 \cdot \rho \cdot v^2 \quad (4)$$

where C_d is the aerodynamical drag coefficient, ρ the air density, and v the wind speed. Since the antennas are fixed to the ground, the wind force will bend the structure, where the stiffness k of the structure determines the amount of flexure x :

$$F_{wind} = -k \cdot x \quad (5)$$

Combination of equations 4 and 5 yields:

$$x = -\frac{C_d \cdot L^2 \cdot \rho \cdot v^2}{2 \cdot k} \quad (6)$$

This is assumed to be valid for any antenna deformation or motion, and to hold for any frequency, and thus for the entire power spectral density (PSD) curve:

$$PSD_{antenna}(\nu) = PSD_{windspeed}(\nu) \cdot H(\nu) \cdot AAF(\nu) \cdot \rho \quad (7)$$

which defines $H(\nu)$ as the transfer function between wind power spectrum and antenna motion power spectrum. The drag coefficient C_d as well as the effective area L^2 of the antenna, and thus the transfer function $H(\nu)$, depend on the orientation of the antenna in azimuth and elevation relative to the wind.

IV. ANALYSIS METHODS

The accelerometer sensitivity was calibrated against gravity around 0.1 Hz, using the antenna to tilt the accelerometers in a controlled way. The sensitivity and frequency response of the read-out electronics was calibrated using a switchable resistor, with which a step-function was fed to the electronics. All relevant measurement data were corrected for accelerometer and electronic effects.

Signals were combined in the time domain, after which the power spectra were calculated. Frequency response corrections were done in the frequency domain. Double integration of

the accelerometer signals, needed to obtain displacement and pointing information, was achieved through division in the frequency domain by $(2\pi\nu)^2$. See the Appendix for details.

A. Extrapolation to Lower Frequencies

The accelerometers are limited in the lowest frequency at which displacements can be measured accurately. Depending on the size of the displacements measured by the accelerometers, and canceling of (tilt-)noise terms in the analysis, the lowest frequency varies between 0.08 and 1 Hz. This frequency limit is well below the lowest eigenfrequency of the antennas, which are 6-7 Hz.

From dynamic structure behaviour, a constant stiffness is expected at frequencies well below the lowest eigenfrequency. This means that the dynamic stiffness of the antenna should reach a constant value in the frequency range between the accelerometer low noise limit and the lowest eigenfrequency. This would show in the plots of the transfer functions H as a flattening of the curve towards lower frequencies. This flattening is seen in all measurements of wind-excited motion. Thus it is possible to determine the (constant) value of the low frequency stiffness from the flat part in the transfer functions, and extrapolate this constant value to lower frequencies, replacing the values in the transfer function affected by accelerometer noise. The scatter in the flat section of the transfer function is used to determine the extrapolation uncertainty, which typically is 6-9%. Subsequently, the extrapolated transfer function is used to calculate antenna performance for the assumed or measured wind spectrum, and the aerodynamic admittance function for 9 m/s wind, as required by the specifications.

B. Pointing Accuracy

The simplest operational mode for the antenna is pointing to a fixed azimuth and elevation, whereby the drives are powered and the brakes are released. In this mode wind effects are best investigated, since any effects of antenna shake due to position updates from the control system are minimal. During sidereal tracking the antenna drives are constantly updating the azimuth and elevation positions, including the azimuth and elevation speed, in order to achieve a smooth tracking motion. Updates are performed at 48 ms intervals, corresponding to a frequency of 20.83 Hz. Antenna motion at frequencies below half this value can be controlled by the drive system, while higher frequencies can only be excited by the drives but not actively corrected.

Wind-induced pointing jitter was investigated for 11 wind-oriented azimuth/elevation combinations, and sidereal tracking was checked for 30 azimuth/elevation combinations spread evenly over the sky. Calm wind conditions were chosen for the sidereal tracking measurements, in order to clearly separate effects due to the drive system from those due to wind. The total pointing accuracy for the antenna is the squared sum of the pointing for high wind conditions without tracking, and the pointing for sidereal tracking during low wind conditions.

The 4 accelerometers on the rim of the BUS were used for deriving the BUS pointing accuracy. The positions for the 4 accelerometers are at the top, right, bottom and left of the BUS,

when looking into the antenna at low elevation. Differential signals between two accelerometers were used to eliminate the large gravity signal common to all accelerometers and being a function of elevation. The cross-elevation and elevation pointing Δ_{XEL} and Δ_{EL} are calculated as follows:

$$\alpha_{XEL} = \frac{a_l - a_r}{x_l - x_r} \quad (8)$$

$$\alpha_{EL} = \frac{a_t - a_b}{y_t - y_b} \quad (9)$$

$$\Delta_{XEL} = \int \int \alpha_{XEL} d^2t \quad (10)$$

$$\Delta_{EL} = \int \int \alpha_{EL} d^2t \quad (11)$$

where α_{XEL} is the cross-elevation angular acceleration, α_{EL} is the elevation angular acceleration, and a_t , a_r , a_l , and a_b are the top, right, left, and bottom accelerometer signals, respectively. The variables x and y are the positions of the accelerometers in coordinates along the elevation axis and perpendicular to the elevation axis, respectively, with the assumed intersection of elevation axis and azimuth axis as the origin. The integration is over the time coordinate t . The total pointing error is given by:

$$\Delta_{TOT} = \sqrt{\Delta_{XEL}^2 + \Delta_{EL}^2} \quad (12)$$

which assumes uncorrelated pointing jitter in elevation and cross-elevation. The accelerometer signals are not significantly affected by noise and other errors down to a frequency of about 0.1 - 0.2 Hz. Below this frequency, the apparent pointing error increases faster than what can be expected from the wind power spectrum and conservative assumptions on the dynamic behaviour of the antenna structure. In combination with optical pointing telescope (OPT) or radiometer measurements, it is possible to measure pointing behaviour for frequencies lower than 0.1 Hz (see Figure 16).

The transfer functions show a flat section below the lowest eigenfrequency. As explained above, this is expected from dynamic antenna behaviour and allows extrapolation of the antenna properties to lower frequencies, as well as the use of the OPT which follows the bulk motion of the reflector in this frequency range. This has been done in the corresponding plots, where the specified wind spectrum has been used to predict antenna properties for time periods up to 15 minutes (0.001 Hz).

Encoder data recorded simultaneously with the wind and accelerometer data were used to calculate the encoder errors, defined as the measured encoder read-out minus the commanded antenna position. Azimuth encoder errors were converted to cross-elevation errors through multiplication with the cosine of the elevation.

C. Primary Reflector Deformation

The combined accelerometer signals measured at the rim of the BUS and at the receiver flange give information about some low-order deformations of the BUS, and thus about the accuracy of the primary reflector surface. Numbers for

the deformations are expressed as boresight components of the deformation at the location of the rim of the BUS. No averaging over the entire reflector surface is attempted. BUS “+” astigmatism is defined as follows:

$$Astig \equiv \int \int a_t + a_b - a_r - a_l d^2t \quad (13)$$

and apex axial motion (AAM) is given by:

$$AAM \equiv \int \int \frac{(a_t + a_r + a_b + a_l)}{4} - a_{rf} d^2t \quad (14)$$

where a_{rf} is the accelerometer signal measured on the receiver flange and in boresight direction.

D. Path length variations

Path length changes measured with the accelerometers reflect the boresight motion of the BUS in the inertial coordinate system, plus the effects of distance changes between the apex and receiver flange:

$$\omega_{xel} = \int \alpha_{xel} dt \quad (15)$$

$$\omega_{el} = \int \alpha_{el} dt \quad (16)$$

$$\alpha_{cf} = -(\omega_{xel}^2 + \omega_{el}^2) \cdot Z_{apex} \quad (17)$$

$$a_{BUS} = \frac{a_t + a_r + a_b + a_l + 4a_{rf}}{8} \quad (18)$$

$$pl = \int \int 2(a_{apex} - \alpha_{cf}) - a_{BUS} d^2t \quad (19)$$

where Z_{apex} is the distance between the apex boresight accelerometer and the azimuth and elevation axes, a_{apex} is the boresight acceleration component at the apex, and α_{cf} is the centrifugal acceleration at the apex due to elevation and cross-elevation motion. The path length calculated this way represents the total optical path length assuming rigid body motion of the BUS and receiver flange, and allowing for boresight displacements of the apex structure. Since the accelerometers measure in the inertial system, and are aligned with the antenna boresight, there is no need to refer to the ground coordinate system or measure mount and yoke path length variations.

E. Structural flexure

Combination of encoder and accelerometer pointing information allows for calculation of antenna structure deformation. The total deformation of the structure between the encoders and the accelerometers on the rim of the BUS was determined by integrating the angular accelerations measured at the BUS to obtain a time series of the angle. Small corrections for timing differences between the encoder and accelerometer equipment were applied. Encoder read-out (AZ_{enc} and EL_{enc} , with the sine and cosine of EL_{enc} , \sin_{el} and \cos_{el}) and the local acceleration g due to gravity are used to calculate the expected accelerations on any point of the antenna with coordinates x,y,z with the intersection of the azimuth and

elevation axes as origin, the coordinate system is fixed to the reflector, with x along the elevation axis, y upward and z along the optical axis for elevation=0, with the axis of measurement of an accelerometer pointing in the direction \vec{dir} :

$$\omega_{enc,az} = \frac{dAZ_{enc}}{dt} \quad (20)$$

$$\omega_{enc,el} = \frac{dEL_{enc}}{dt} \quad (21)$$

$$\alpha_{enc,az} = \frac{d\omega_{enc,az}}{dt} \quad (22)$$

$$\alpha_{enc,el} = \frac{d\omega_{enc,el}}{dt} \quad (23)$$

$$\vec{g} = g \cdot \begin{pmatrix} 0 \\ -\cos_{el} \\ -\sin_{el} \end{pmatrix} \quad (24)$$

$$\vec{cf}_{el} = \omega_{enc,el}^2 \cdot \begin{pmatrix} 0 \\ y \\ z \end{pmatrix} \quad (25)$$

$$\vec{cf}_{az} = \omega_{enc,az}^2 \cdot \begin{pmatrix} x \\ y \cdot \sin_{el}^2 - z \cdot \sin_{el} \cdot \cos_{el} \\ -y \cdot \sin_{el} \cos_{el} + z \cdot \cos_{el}^2 \end{pmatrix} \quad (26)$$

$$\vec{ang}_{el} = \alpha_{el} \cdot \begin{pmatrix} 0 \\ z \\ y \end{pmatrix} \quad (27)$$

$$\vec{ang}_{az} = \alpha_{az} \cdot \begin{pmatrix} y \cdot \sin_{el} - z \cdot \cos_{el} \\ x \cdot \sin_{el} \\ x \cdot \cos_{el} \end{pmatrix} \quad (28)$$

$$\vec{accel} = \vec{g} + \vec{cf}_{el} + \vec{cf}_{az} + \vec{ang}_{el} + \vec{ang}_{az} \quad (29)$$

$$sig_{accel} = \vec{accel} \cdot \begin{pmatrix} dir_x \\ dir_y \\ dir_z \end{pmatrix} \quad (30)$$

The centrifugal accelerations due to elevation and azimuth slews are given by \vec{cf}_{el} and \vec{cf}_{az} respectively, and the accelerations due to angular accelerations in elevation and azimuth are given by \vec{ang}_{el} and \vec{ang}_{az} respectively. The expected acceleration thus calculated is then convolved with the time response TR of the read-out equipment, to obtain a time series of expected accelerations which can be directly compared to the measured accelerations:

$$\alpha_{expected} = sig_{accel} * TR \quad (31)$$

where $*$ denotes convolution, and $\alpha_{expected}$ is the expected bandwidth filtered accelerometer signal.

Both measured and expected accelerometer signals are treated in the same way to calculate antenna pointing. The data are resampled to a common time grid, small corrections for accelerometer sensitivity and integration constants are applied to make the expected and measured antenna pointing

match, and the difference between the measured and expected pointing is plotted together with a scaled curve of the angular acceleration during the fast motion of the antenna. The scaling factor required to make the acceleration curve match to the structure flexure curve is the measure of flexure of the antenna structure. Since the flexure due to an inertial acceleration scales with the acceleration and the mass of the antenna, and gravitational flexure of the antenna also scales with the mass of the antenna, the numbers for the structure flexure give an indication of generic structure stiffness against gravitational effects as well.

V. RESULTS

The measurement results obtained at the ATF site were used to derive environmentally independent antenna properties where possible. The Statement of Work and Specifications for the ALMA prototype antennas (SoW) specifies antenna performance for the environmental conditions at the ALMA site, where in particular the wind power spectrum and air density are of relevance for this investigation. Using the transfer functions derived at the ATF site, antenna performance was calculated for conditions representative at the ALMA site and defined in the SoW. The main differences between the ATF and SoW conditions are for air pressure (SoW: 550 mBar), wind speed (ATF: variable between 0.05 m/s and exceeding 20 m/s, SoW: 9 m/s) and wind power spectrum (SoW: more power at lower frequencies than observed at ATF).

A. Pointing

Table I summarises the dynamic pointing performance of the AEC and VertexRSI antennas. Measurement noise is typically sub- μm scale at 0.1 Hz, and several nm at 1 Hz. Uncertainties in the results are generated by the variation of the measurement results over different elevation and azimuth positions, uncertainties in the determination of the wind power spectrum as experienced by the antennas at the time of measurement, and extrapolation to lower frequencies. Where applicable, these three individual contributions to the measurement results are shown in Table I.

1) *Stationary pointing*: Figure 7 shows the transfer functions H between wind PSD and BUS pointing PSD for the VertexRSI antenna, as defined in §III-B. The red and green curves show elevation and cross-elevation pointing respectively. The low-frequency values of the red and green curves, here shown for frequencies above 1 Hz, show the expected behaviour below the lowest eigenfrequency and can be extrapolated to 0 Hz. Similar curves and behaviour are observed for the AEC antenna, though not shown here.

Wind-induced pointing jitter is dominated for both antennas by elevation motion. Encoder errors do not exceed 0.14 arcsec for the VertexRSI antenna, and remain below 0.07 arcsec for the AEC antenna. Both antennas show azimuth-dependent pointing performance, where pointing jitter is larger when the antenna is looking into the wind, and smallest for wind coming from sideways-behind. These results most likely reflect the smaller projected area of the antenna when viewed from the side, and the higher drag coefficient of the ‘‘cup’’ formed by the primary mirror and BUS when viewed from the front.

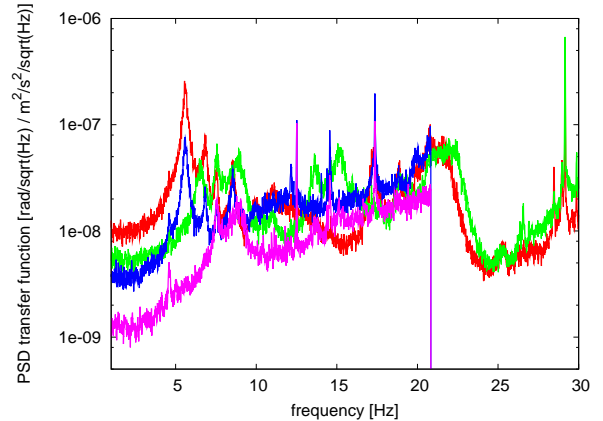


Fig. 7. VertexRSI antenna elevation (red) and cross-elevation (green) pointing transfer functions for wind excitation. The blue and magenta curves show the encoder error transfer functions for elevation and cross-elevation respectively.

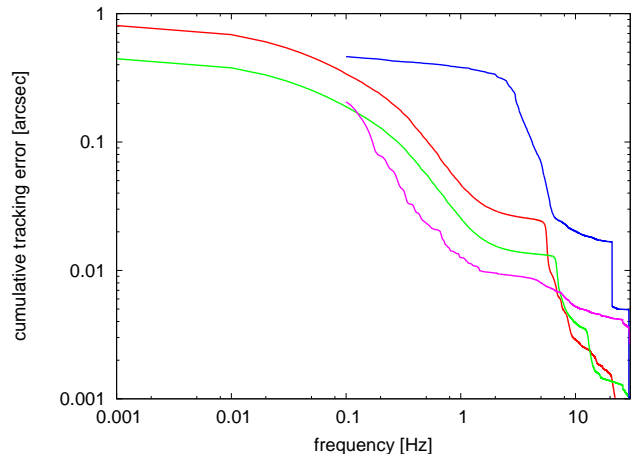


Fig. 8. RMS tracking jitter for VertexRSI and AEC antennas. The extrapolated wind-induced jitter for conditions specified in the SoW is shown as red (VertexRSI) and green (AEC) curves. Pointing stability during sidereal tracking is given by the blue (VertexRSI) and magenta (AEC) curves. For sidereal tracking under windy conditions, both curves must be combined.

2) *Sidereal Tracking*: Tracking jitter of the VertexRSI antenna is for a significant part due to elevation motion, with large contribution in the 3-6 Hz range. Total tracking jitter over timescales of 10 seconds amounts to 0.47 ± 0.11 (spread) arcsec average. Largest jitter is observed for low elevation in the south-east and south-west, and minimum tracking jitter is seen while crossing the meridian. Total tracking jitter for the AEC antenna, over timescales of 10 seconds, amounts to 0.22 ± 0.08 (spread) arcsec average. As for the VertexRSI antenna, the sidereal tracking jitter depends on the antenna pointing.

3) *Combined Wind and Tracking*: The pointing jitter due to wind and due to sidereal tracking are assumed to be uncorrelated, in which case the cumulative pointing error curves can be added quadratically. A check of an independent measurement with high wind and sidereal tracking showed that this assumption is valid. Since no tracking jitter at 0.001 Hz

TABLE I
POINTING

Pointing type	VertexRSI	AEC
stationary, windy conditions	$0.81 \pm 0.24^a \pm 0.05^b \pm 0.20^c$ arcsec	$0.45 \pm 0.10^a \pm 0.02^b \pm 0.11^c$ arcsec
sidereal tracking, no wind	0.47 ± 0.11^a arcsec	0.22 ± 0.08^a arcsec
tracking, windy conditions, 0.1 Hz	$0.58 \pm 0.15^a \pm 0.08^c$ arcsec	$0.29 \pm 0.09^a \pm 0.05^c$ arcsec
tracking, windy conditions, 0.001 Hz	$0.94 \pm 0.26^a \pm 0.05^b \pm 0.20^c$ arcsec	$0.50 \pm 0.13^a \pm 0.02^b \pm 0.11^c$ arcsec
on-the-fly, 0.5 deg/s, 1 Hz	1.7 ± 0.7 arcsec	0.5 ± 0.3 arcsec
on-the-fly ^d , 0.5 deg/s, 1 Hz		0.372 ± 0.015 arcsec
on-the-fly, 0.05 deg/s, 1 Hz	0.8 ± 0.5 arcsec	0.231 ± 0.007 arcsec

^a Spread over different azimuth/elevation combinations.

^b Extrapolation error for the transfer function.

^c Uncertainty in wind power spectrum determination.

^d Ignoring AEC apex rotation.

could be measured, a conservative value equal to the observed tracking jitter at 0.1 Hz is used.

Figure 8 shows the wind induced and sidereal tracking jitter for both antennas. At 0.1 Hz, the combined wind and tracking jitter was calculated from direct measurements, while at 0.001 Hz the pointing jitter was derived from the extrapolated transfer function. The red and green curves show the wind-induced pointing jitter for the VertexRSI and AEC antennas respectively, and the blue and magenta curves show the sidereal tracking stability.

4) *Pointing During OTF*: During OTF scanning the time between switches in scan direction was typically 10 seconds. With a few seconds settling time for the antenna after each switch, only a few seconds remained during which representative measurements could be taken. This limited the effective lowest frequency at which antenna performance could be calculated to 1 Hz.

For the VertexRSI antenna, the azimuth and elevation at which the scan was performed had large impact on the pointing stability during the scan. On the other hand, the AEC antenna measurements were affected for some parts of the scan by apex rotation feeding back to the BUS motion, an effect which died out about a minute into the scan. Both effects resulted in a large spread of the measurement results, represented in the standard deviation stated in Table I.

B. BUS deformations

Table II summarises the results for deformation of the BUS. For both antennas, surface stability is dominated by the stiffness of the BUS for wind excitation, and apex axial motion and astigmatism are each below $1 \mu\text{m}$ RMS for sidereal tracking.

During a fast switch of antenna pointing, the accelerometers show a deformation of the BUS rim of nearly 1.4 mm astigmatism peak-to-peak for the VertexRSI antenna, and nearly 4 mm for the AEC antenna. During a fast switch, no astronomical data is recorded, so deformation of the BUS is no concern, as long as recovery of the shape is fast enough after the antenna pointing has stabilised. Astigmatism recorded 1.5 seconds after the fast switch started, up to the next switch 8.5 seconds later, remains well below $2 \mu\text{m}$ peak-to-peak for the VertexRSI antenna, and below $15 \mu\text{m}$ peak-to-peak for the AEC antenna, after removal of a low order polynomial. The polynomial removes the large noise component in the

accelerometer signals at the lowest frequencies. In this case, the crude removal of the noise component is justified, but the resulting number for the remaining astigmatism should only be used as an order of magnitude indication.

Five seconds after a fast switch for the AEC antenna, the astigmatism had died down to typically $1 \mu\text{m}$ peak-to-peak. The reason for the large peak-to-peak variation is the 5 Hz resonance of the apex structure which takes some time to die out. During apex rotation, the BUS gets deformed through the feed legs bending which drive the apex rotation.

BUS astigmatism during the fast OTF scan, with 0.5 deg/s scan rate, averages to $0.9 \pm 0.3 \mu\text{m}$ RMS over timescales of 1 second for the VertexRSI antenna, and $4 \pm 2 \mu\text{m}$ RMS for the AEC antenna. Surface stability is affected for some parts of the scan by apex rotation feeding back to the BUS motion. The spread of $2 \mu\text{m}$ (1σ) reflects this variable surface stability. Ignoring the parts of the scan affected by apex rotation, the numbers reduce to $3.19 \pm 0.14 \mu\text{m}$. When the scan rate is reduced to 0.05 deg/s, for interferometric mosaicking, BUS astigmatism averages to $0.27 \pm 0.09 \mu\text{m}$ RMS over timescales of 1 second for the VertexRSI antenna, and $2.2 \pm 0.2 \mu\text{m}$ RMS for the AEC antenna.

BUS apex axial motion stability during the fast OTF scan, with 0.5 deg/s scan rate, averages to $1.9 \pm 0.6 \mu\text{m}$ RMS over timescales of 1 second for the VertexRSI antenna, and 2 to 20 μm RMS for the AEC antenna. Also here, the apex rotation significantly affected the surface stability of the BUS. Ignoring the parts of the scan affected by apex rotation, the numbers reduce to $1.94 \pm 0.08 \mu\text{m}$. When the scan rate is reduced to 0.05 deg/s, for interferometric mosaicking, VertexRSI BUS AAM stability averages to $1.0 \pm 0.3 \mu\text{m}$ RMS over timescales of 1 second, and AEC BUS AAM stability averages to $1.4 \pm 0.2 \mu\text{m}$ RMS.

Overall, dynamic BUS deformations due to motion of the antennas are small if the apex rotation effect can be ignored.

C. Path Length

Wind induced path length variations for both antennas amount to $6 \mu\text{m}$ RMS over timescales of 15 minutes, see Table III for an overview

For sidereal tracking, path length variations over timescales of 1 second remain below $2 \mu\text{m}$ for the VertexRSI antenna, and below $0.5 \mu\text{m}$ for the AEC antenna.

TABLE II
BUS DEFORMATION

Type of deformation	VertexRSI	AEC
astigmatism, wind-induced, 0.001 Hz	5.3 μm	6 μm
astigmatism, 1.5 - 10 s after fast-switch	2 μm peak-to-peak	15 μm peak-to-peak
astigmatism, OTF 0.5 deg/s, 1 Hz	0.9 \pm 0.3 μm	4 \pm 2 μm
astigmatism, OTF ^a 0.5 deg/s, 1 Hz		3.19 \pm 0.09 μm
astigmatism, OTF 0.05 deg/s, 1 Hz	0.27 \pm 0.09 μm	2.2 \pm 0.9 μm
AAM, wind-induced, 0.001 Hz	2.2 μm	5 μm
AAM, OTF, 0.5 deg/s, 1 Hz	1.9 \pm 0.6 μm	2 - 20 μm
AAM, OTF ^a , 0.5 deg/s, 1 Hz		1.94 \pm 0.08 μm
AAM, OTF, 0.05 deg/s, 1 Hz	1.0 \pm 0.3 μm	1.4 \pm 0.2 μm
AAM and astigmatism, tracking induced, 0.1 Hz	< 1 μm	< 1 μm

^a Ignoring AEC apex rotation.

TABLE III
PATH LENGTH

Source of path length variations	VertexRSI	AEC
wind-induced, 0.001 Hz	6 μm	6 μm
sidereal tracking, 1 Hz	2 μm	0.5 μm
OTF, 0.5 deg/s, 1 Hz	12 \pm 7 μm	3.3 \pm 2.9 μm
OTF ^a , 0.5 deg/s, 1 Hz		2.2 \pm 0.5 μm
OTF, 0.05 deg/s, 1 Hz	3.1 \pm 1.0 μm	0.7 \pm 0.02 ^b μm

^a Ignoring AEC apex rotation.

^b BUS only.

TABLE IV
STRUCTURAL FLEXURE

direction	VertexRSI	AEC
cross-elevation	2.1 arcsec/(deg/s ²)	1.6 arcsec/(deg/s ²)
elevation	2.8 arcsec/(deg/s ²)	2.1 arcsec/(deg/s ²)

Total path length stability during the fast OTF scan, with 0.5 deg/s scan rate, averages for the VertexRSI antenna to 12 \pm 7 μm RMS over timescales of 1 second. Depending on the azimuth, path length stability may be as bad as 20 μm RMS. The AEC antenna path length jitter averages to 3.3 \pm 2.9 μm RMS. The path length stability is affected for some parts of the scan by apex rotation feeding back to the BUS motion, as well as changing the distance between BUS and apex. The spread of 2.9 μm (1 σ) reflects this variable path length stability. Ignoring the parts of the scan which are affected by apex rotation, the numbers reduce to 2.2 \pm 0.5 μm .

When the scan rate is reduced to 0.05 deg/s, for VertexRSI antenna interferometric mosaicking, total path length stability averages to 3.1 \pm 1.0 μm RMS over timescales of 1 second, and 0.70 \pm 0.02 μm RMS for the AEC antenna. Note that for the AEC antenna, this number covers the BUS boresight path length stability only, therefore it was not possible to measure the full apex motion accurately.

D. Structural Flexure

The pointing difference between encoders and accelerometers scales well with the angular acceleration. The scaling factor is the antenna stiffness for this type of load, and is summarised in Table IV. Structure flexure affects pointing accuracy during OTF scanning as a result of large angular accelerations during scan reversal, which affect pointing by 0.8 arcsec in elevation, and 0.6 arcsec in cross-elevation for the

VertexRSI antenna, and 0.6 arcsec and 0.5 arcsec, respectively, for the AEC antenna. Since the driving force for the deformation is an acceleration, the numbers are also indicative for the stiffness of the structure for gravity deformation, though the exact numbers there will be different and could not be derived from the measurements performed during this investigation.

E. Vibration Environment

1) *Eigenfrequencies*: Figure 9 illustrates some of the VertexRSI antenna locked rotor eigenfrequencies, and Figure 10 illustrates some of the AEC antenna. The antennas were in shutdown mode at approximately 45 degrees elevation. The figures show the elevation, cross-elevation, and boresight motion of the BUS. The lowest significant eigenfrequency is visible in elevation and boresight at 5.57 Hz (VertexRSI antenna) and 6.8 Hz (AEC antenna). There is a small peak visible at a frequency of 4.68 Hz for the VertexRSI antenna, which is the print-through of the apex structure rotation mode, along an axis through boresight.

Some equipment installed on submillimeter radio telescopes, in particular bolometers, may be sensitive to vibration. The accelerometers provide a very accurate measure of the vibration environment provided by the antenna. Two locations on the antenna were investigated in some detail: the receiver flange, and the apex structure. For both locations, 3-axis accelerometer measurements are available for a variety of conditions.

Under windy conditions, without sidereal tracking, the RMS acceleration on the VertexRSI antenna receiver flange, combining all 3 axes, amounts to 0.48 mm/s². For the apex structure, the corresponding number is 4.4 mm/s². For similar conditions, the AEC antenna has vibration levels of 0.40 mm/s² at the receiver flange, and 3.6 mm/s² at the apex structure.

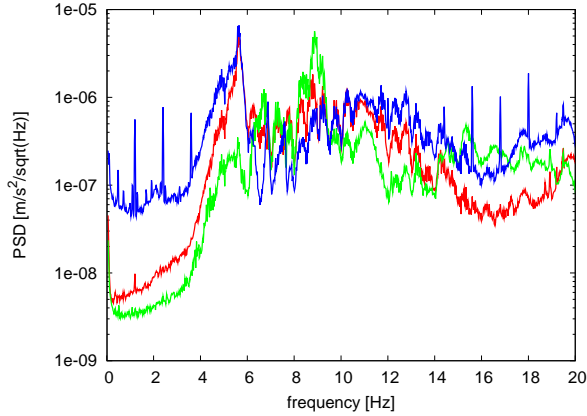


Fig. 9. VertexRSI elevation (red), cross-elevation (green) and boresight (blue) motion power spectral density. The antenna was in shutdown mode at 45 degrees elevation during a typical day at the ATF. The curves for the elevation and cross-elevation motion are in units $\text{rad/s}^2/\sqrt{\text{Hz}}$. The spikes in the boresight motion curve are the result of vibrations of the receiver flange introduced by the cryogenic pump for the receivers.

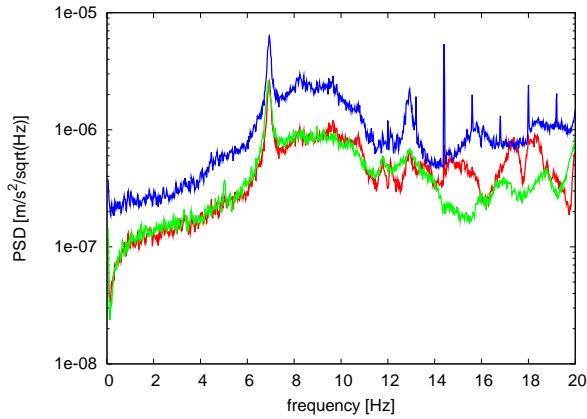


Fig. 10. AEC elevation (red), cross-elevation (green) and boresight (blue) motion power spectral density. The antenna was in shutdown mode at 45 degrees elevation during a typical day at the ATF. The curves for the elevation and cross-elevation motion are in units $\text{rad/s}^2/\sqrt{\text{Hz}}$.

For the VertexRSI antenna, Figures 11 and 12 show the X (red, along the elevation axis), Y (green, perpendicular to the elevation axis), and Z (blue, boresight) PSDs of the acceleration, for the receiver flange and apex, respectively. The apex structure rotates slightly around its own axis, with a frequency of approximately 4.7 Hz. The amplitude of the rotation is small, but affects the vibration environment depending on the location of the accelerometer. For this specific measurement, the accelerometers were placed near the edge of the apex cylinder, and makes the Y measurement sensitive to rotation as well as displacement.

For the AEC antenna, Figures 13 and 14 show the X (red), Y (green), and Z (blue) PSDs of the acceleration, for the

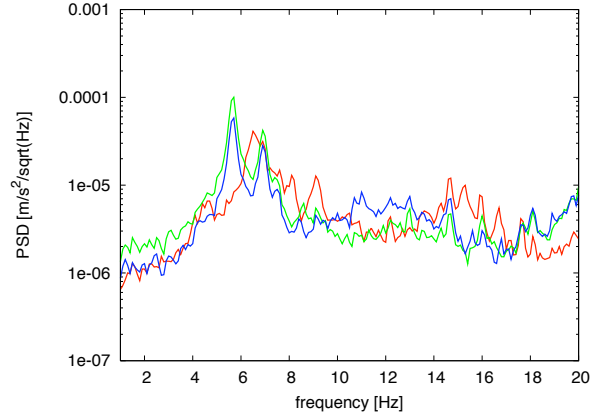


Fig. 11. VertexRSI receiver flange acceleration PSD. Red, green and blue curves show the X, Y and Z components of the acceleration. Wind was approximately 9 m/s, and elevation was 45 degrees.

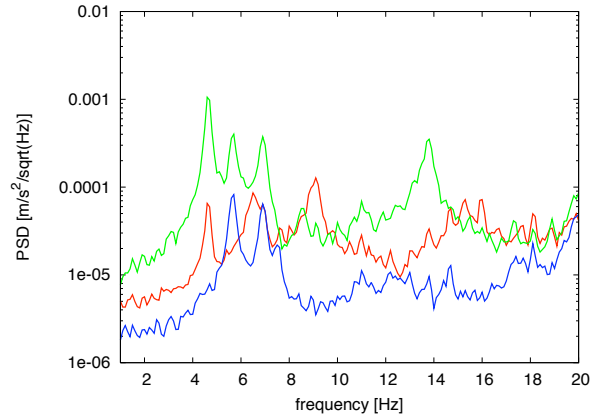


Fig. 12. VertexRSI apex acceleration PSD for the same conditions as those shown in Figure 11.

receiver flange and apex, respectively. Also the AEC antenna apex structure rotates somewhat around its own axis, with a frequency of 5.0 Hz. For this specific measurement, the accelerometers were placed on the outer part of the apex cylinder, and makes the X measurement sensitive to rotation as well as displacement.

2) *External Vibration Pick-Up*: During performance testing it became clear that the antennas are sensitive to vibrations caused by motion of the other antennas, which are transmitted through the ground. In order to test this sensitivity in a more controlled way, the Mitsubishi antenna, located 35 m to the west of the VertexRSI antenna, was instructed to make a 2 degree azimuth slew, while accelerometers monitored the motion of the VertexRSI antenna. The move caused peak-to-peak pointing errors of 0.30 arcsec in elevation, 0.40 arcsec in cross-elevation, and $2.9 \mu\text{m}$ in boresight motion. The elevation for the VertexRSI antenna was 30 degrees.

Vibration transfer from the VertexRSI antenna to the AEC

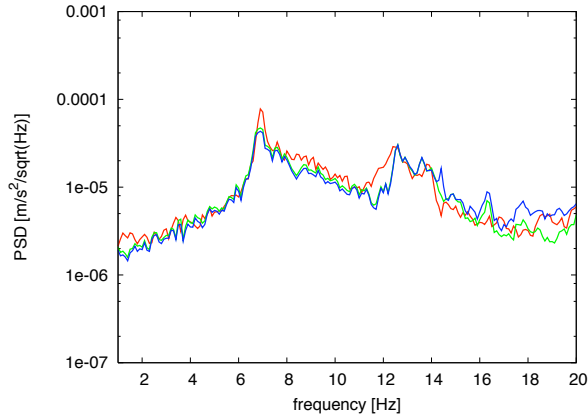


Fig. 13. AEC receiver flange acceleration PSD. Red, green and blue curves show the X, Y and Z components of the acceleration. Wind was approximately 9 m/s, and elevation was 45 degrees.

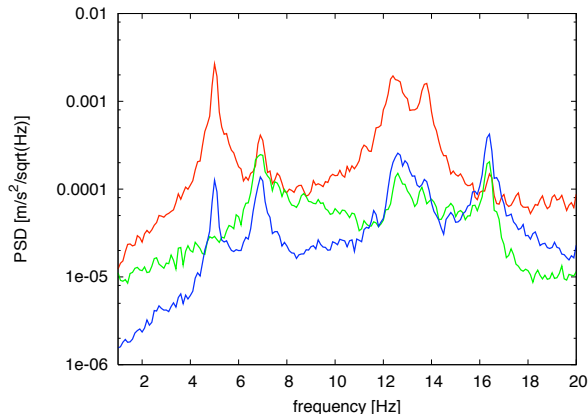


Fig. 14. AEC apex acceleration PSD for the same conditions as those shown in Figure 13.

antenna, also placed 35 m apart, was investigated by making the VertexRSI antenna perform fast switches with 1 degree offset in both azimuth and elevation, and by making it perform an interferometric OTF scan at 0.05 deg/s. The elevation of the AEC antenna was 30 and 10 degrees respectively, during the tests. The accelerometers mounted on the AEC antenna measured RMS motion during the fast switching of 0.043 arcsec in elevation, 0.012 arcsec in cross elevation, and 0.7 μm RMS in boresight motion. However, since the motion is peaked during the acceleration of the VertexRSI antenna, and undetectable a few seconds after the move, the peak-to-peak values of the pointing errors are of interest too. Peak-to-peak motion was 0.29 arcsec in elevation, 0.13 arcsec in cross-elevation, and 5.3 μm in boresight motion. For the interferometric OTF scan, the numbers are 0.016 arcsec RMS or 0.23 arcsec peak-to-peak in elevation, 0.011 arcsec RMS or 0.31 arcsec peak-to-peak in cross-elevation, and 0.29 μm RMS or 4.4 μm peak-to-peak boresight motion.

These numbers are presented to give an impression of the impact of the motion of nearby antennas. The tests were far too limited to draw any further conclusions, and would depend critically on the soil conditions at the ALMA and ATF sites.

VI. DISCUSSION

All wind-related antenna data obtained at the ATF have been analysed in such a way as to represent antenna properties, independent of the shape of the wind spectrum, or wind speed. With these antenna properties, it is possible to predict wind-driven antenna performance for any wind speed, wind spectrum, and air density, even for conditions not encountered during antenna testing. One of the expected and observed properties of the transfer functions as defined in Eqn. 7 allows a simple extrapolation of antenna properties measured between 0.1 Hz and a few Hz to values below 0.1 Hz, and in principle to 0 Hz. In the frequency domain this is a simple exercise, but in time domain it corresponds to extrapolation of antenna properties measured at timescales of seconds to timescales of tens of minutes or longer. Since the wind contains the majority of its power at low frequencies, this extrapolation is extremely useful for the prediction of the overall wind performance of the antenna.

Besides extrapolation to lower frequencies, the transfer functions can be used to scale antenna performance measured under uncontrolled wind conditions to any known and well-defined wind spectrum. The antennas have been designed to meet the specifications for a given reference spectrum, which was given in the SoW. In order to test compliance with the specifications, the measured antenna performance must be scaled to this SoW reference spectrum, a straightforward task, which does not leave much room for speculation but provides hard numbers instead.

One must realise, however, that the numbers for antenna performance obtained using the wind transfer functions are valid only under the assumptions made here, i.e. that wind effects dominate the performance. For timescales of seconds to tens of seconds, this may very well be the case, but when extrapolated to timescales of tens of minutes to hours, other effects such as thermal effects may contribute significantly to the total antenna performance at these timescales.

A. Apex Rotation: Experiences with Accelerometer Placement and as Tool for Troubleshooting

The results presented in this paper are for pointing stability as derived from motion of the BUS only. The position of the subreflector determines how the primary focus image is projected at the secondary focus, and shake of the subreflector with respect to the BUS may introduce additional pointing variations.

During the measurements, it became clear that the apex structures of both antennas rotate about the boresight axis. With only 3 accelerometers at the apex structure, it was no longer possible to discern between rotations and translations of the subreflector. At the prime focus the plate scale is 34 arcsec/mm, which requires stability of the apex structure to be on the order of a few tens of μm . Using reconfigured

accelerometers on one of the antennas, it was possible to distinguish between rotation and translation in one dimension. This revealed that for some resonance modes, the pointing errors introduced by the BUS were compensated by those introduced due to subreflector translation. Thus, the total pointing error projected at the receiver flange may be larger or smaller than the pointing stability derived from the BUS.

Excessive rotation of the AEC antenna apex structure highlighted both strengths and weaknesses of the accelerometer concept used in these investigations. The main weakness was the inability of the 3-accelerometer set-up on the apex structure to discern between translation and rotation of the structure. Since the apex structure rotation was not foreseen at the time the accelerometer system was designed, no provisions were made to distinguish between rotation and translation. As it turned out, the rotation was so large that careful on-axis placement of all three accelerometers would have been necessary, not a trivial task given the dimensions of the accelerometers.

The strength of the accelerometer system was demonstrated when one of the accelerometers at the apex was reconfigured to allow distinction between rotation and translation (at the cost of the ability to measure one displacement dimension). With the new configuration, it could be determined that the detected accelerations were indeed caused by rotation of the apex structure, that the rotation was off-axis, and that the rotation axis shifted with elevation. This off-axis rotation of the apex structure translates into a pointing error of up to 1 arcsec peak-to-peak in cross-elevation, provided that the rotation axis is parallel to the boresight axis (which could not be confirmed). In summary, this sequence of tests illustrated the versatility of the accelerometer system as a diagnostic tool for troubleshooting.

B. Antenna Wake Turbulence: Spin-Off and Implications for Compact Array Configurations

The SoW has a primary operating condition for antenna wake conditions, with an average wind speed of 7 m/s instead of 9 m/s for non-wake conditions, and a variable component of 4 times the SoW reference wind spectrum. Analysis of wind data measured in the wake of the 3 antennas placed at the ATF, and OPT pointing stability with the AEC antenna in the wake of both the Mitsubishi and VertexRSI antennas, has revealed detailed properties of the antenna wake turbulence.

Figure 15 shows the effect antenna wake turbulence has on the undisturbed wind, as measured with the sonic anemometer, for wind passing the Mitsubishi prototype antenna. The measured PSD downwind of the antenna was scaled with the average wind speed, and divided by the average scaled PSD for wind coming from unobstructed directions. The curve shows how the unobstructed wind is affected by the antenna, at a distance of approximately 30 m. The scaling factor for the high frequencies is approximately flat with frequency, at a value of 2.5, but the low frequency part of the spectrum is not affected by the same amount. Turn-over occurs in the range around 0.1 Hz. This means that the turbulence introduced in the antenna wake has frequencies of 0.1 Hz and higher, and

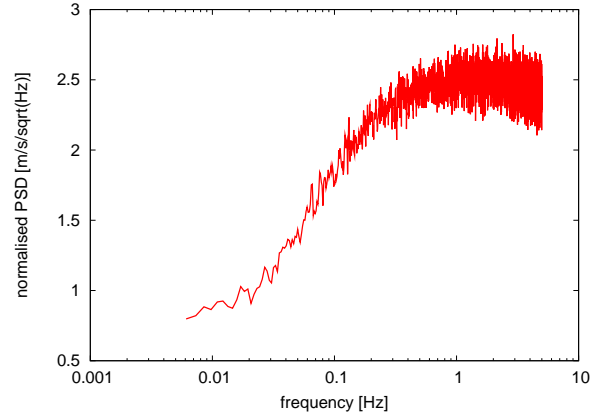


Fig. 15. Antenna wake turbulence as measured with the sonic anemometer, for wind passing the Mitsubishi prototype antenna. The PSD was scaled with the wind speed, and divided by the average scaled PSD for wind coming from unobstructed directions.

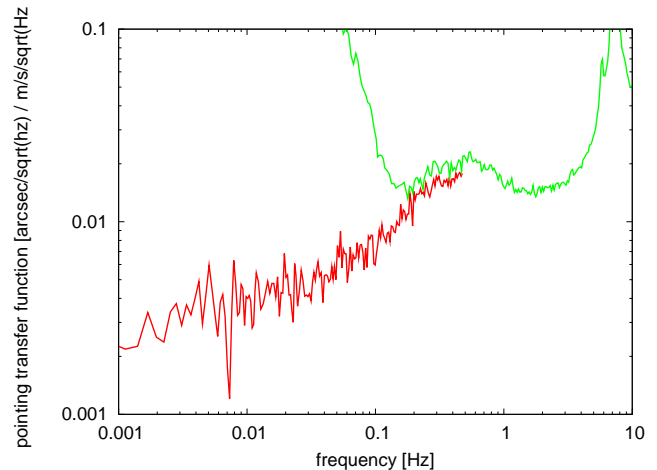


Fig. 16. Antenna wake turbulence and AEC antenna resonance as measured with the OPT and accelerometers, for wind passing the Mitsubishi and VertexRSI prototype antennae. The PSD for elevation pointing was scaled with the wind speed, and divided by the PSD of the wind during the measurement. The green curve is measured with the accelerometers, the red curve with the optical pointing telescope. Wind was approximately 12 m/s average.

will at these frequencies shake any antenna placed in this wake a factor 2.5 more than in the absence of the extra turbulence.

Figure 16 shows the antenna wake turbulence as measured on the AEC antenna with the accelerometers and the OPT simultaneously. The wind was predominantly from the west, passing over the Mitsubishi and VertexRSI antennas. The high frequency part of the plot is dominated by antenna resonances and vortex shedding off of the other antennas, measured with the accelerometers. Below the lowest eigenfrequency around 7 Hz, the curve is expected to flatten, which is also seen down to frequencies of about 0.2 Hz. Below this frequency, the accelerometers are affected by noise. The simultaneous measurements with the OPT, tracking on Polaris, show an overlap up to 0.7 Hz, and are not affected by low frequency noise, and thus valid down to the lowest frequencies.

Note the good overlap of the curves in the frequency range between 0.2 and 0.7 Hz, as expected under the assumption that both the OPT and accelerometers see the same BUS motion. The effects of combined Mitsubishi and VertexRSI turbulence are also here clearly visible, with a turn-over frequency around 0.1 Hz. The magnitude of the high frequency turbulence gain is approximately a factor 4 to 5.

Thus the SoW requirement for 4 times the wind spectrum (which translates to 2 times the wind spectrum in the units used in the figures here, $m/s/\sqrt{Hz}$) in the wake of an antenna is valid, but only for frequencies above 0.1 Hz. It is also clear from the ATF antenna wake turbulence, that the level of the turbulence depends on the distance to the antenna, and that the effects of multiple antennae appear to be multiplicative.

Since the low frequency (0.001 Hz) antenna wind performance is dominated by the low frequency stiffness of the antenna for wind excitation, the resonances, which are all well above 1 Hz, and the wake turbulence generated by nearby antennas, at frequencies above approximately 0.1 Hz, do not significantly affect wind-related antenna performance for timescales of 15 minutes (0.001 Hz). The cumulative effect of several antennas upwind may, however, not be negligible as seen with the combined Mitsubishi and VertexRSI wake turbulence. Nor will the wake turbulence be negligible any longer when a properly functioning metrology system suppresses the low frequency (below 0.1 Hz) wind buffeting of the antennas, or when antenna performance (beyond the requirements) at frequencies above 0.1 Hz is an issue.

VII. CONCLUSIONS

A. Accelerometers

Seismic accelerometers mounted on the back-up structures of large reflector antennas are capable of characterising all relevant BUS rigid body motions, and a few of its low-order deformation modes. Independently of any external sources to the antenna, and even for antennas without receivers, it is possible to derive the dynamical behaviour of the performance parameters of an antenna, such as pointing accuracy, primary reflector surface stability, and path length stability. The accuracy at which performance parameters can be measured is a function of frequency, and typically at the sub- μm and sub-arcsecond level for frequencies above 0.1 Hz.

In combination with wind measurements, antenna performance for windy conditions can safely be extrapolated to frequencies well below the limit of 0.1 Hz imposed by noise in the accelerometer data. The validity of this extrapolation has been demonstrated with the use of an optical pointing telescope, not limited by the low-frequency noise.

In addition to performance testing, the robust accelerometer system has proven to be well suited for troubleshooting of unexpected antenna behaviour, such as large and off-axis apex structure rotation for the AEC antenna, and servo-tuning issues for the VertexRSI antenna.

B. Wind-Driven Performance

Performance of the antennas for windy conditions was a major design driver. In spite of the very different wind

conditions at the antenna test site and the ALMA site, it was possible to accurately predict performance for the ALMA site based on measurements performed at the ATF. The key to this extrapolation is careful characterisation of the wind at the sites, in particular at the ATF site. Wind-driven performance as measured on the antennas was combined with the wind characteristics during the time of measurement, which allowed calculation of wind-independent antenna properties, allowing calculation of antenna performance for any wind condition.

As a spin-off of the investigations, antenna wake turbulence at a typical distance of 30 - 50 m was determined; which is useful information for calculation of antenna performance in the compact configuration.

C. Antenna Performance

Antenna performance as measured with the accelerometers complements other performance measurements, such as optical and radio pointing, and holography. The full performance of the antennas could not be determined with any of the individual methods, but a combination of them gives confidence in the completeness of the test results.

During design, antenna performance was calculated from the sum of individual contributions to the total error budget. The performance numbers presented in this paper are best interpreted in the context of the corresponding error budget contributions used for antenna design. Table V gives the measured performance for each antenna, and the calculated error budget entry as taken from the design documentation where available [3].

ACKNOWLEDGMENT

The authors would like to thank Nobuharu Ukita (National Astronomical Observatory of Japan) and David R. Smith (Merlab) for valuable discussions on the design of the accelerometer system and analysis of the measurements, Angel Otarola and Juan Pablo Perez Beaupuits (ESO) for providing wind data for the ALMA site, and Fritz Stauffer and Nicholas Emerson (NRAO) for valuable support at the ATF.

REFERENCES

- [1] H. J. Kärcher and J. W. M. Baars, "The design of the Large Millimeter Telescope / Gran Telescopio Milimétrico (LMT/GTM)", *Proceedings SPIE*, **4015**, 2000, pp. 155-168.
- [2] J. W. M. Baars, "The Measurement of large Antennas with cosmic Radio Sources", *IEEE Trans. Antennas Propagation*, **21**, 1973, pp. 461-474.
- [3] J. G. Mangum, J. W. M. Baars, A. Greve, R. Lucas, R. Snel, P. T. Wallace and M. Holdaway, "Evaluation of the ALMA Prototype Antennas", *Publ. Astron. Soc. of the Pacific*, **118**, 2006, pp. 1257-1301.
- [4] D. R. Smith, P. Avitabile, G. Gwaltney, M. Cho and M. Sheehan, "Wind-Induced Structural Response of a Large Telescope", *Proceedings SPIE*, **5495**, 2004, p. 258.
- [5] N. Ukita and M. Ikeda, "Antenna Vibration Measurements with Accelerometers", 2002, URSI General Assembly (Maastricht), 2002, p. 1958.
- [6] N. Ukita, M. Saito, H. Ezawa, B. Ikenoue, H. Ishizaki, H. Iwashita, N. Yamaguchi, T. Hayakawa, "Design and performance of the ALMA-J prototype antenna", *Proceedings SPIE*, **5489**, 2004, pp. 1085-1093.
- [7] F. Zernike, "Diffraction Theory of the Knife-Edge Test and its Improved Form, The Phase-Contrast Method", *Monthly Not. Roy. Astron. Soc.*, **94**, 1934, p. 377.
- [8] A. Greve and J. G. Mangum, "Mechanical Measurements of the ALMA Prototype Antennas", *IEEE Antennas and Propagation Magazine*, submitted 2006.

TABLE V
WIND POINTING

	VertexRSI	AEC
Pointing accuracy (wind only)	0.81 arcsec	0.45 arcsec
Pointing accuracy (wind only) error budget	0.035 arcsec	0.35 arcsec
Pointing accuracy (wind + tracking)	0.94 arcsec	0.50 arcsec
Pointing accuracy offset pointing requirement	0.6 arcsec	0.6 arcsec
Primary reflector surface stability, wind effects (astigmatism + AAM, at edge of BUS)	5.3 + 2.2 μm	6 + 5 μm
Primary reflector surface stability, wind effects error budget	8.4 μm	2.1 μm
Primary reflector surface stability, overall requirement	25 μm	25 μm
Path length stability, wind effects	6 μm	6 μm
Path length stability, wind effects error budget	7.6 μm	3.5 μm
Path length stability, requirement total non-repeatable residual delay	15 μm	15 μm
Structure flexure cross-elevation	2.1 arcsec/(deg/s ²)	1.6 arcsec/(deg/s ²)
Structure flexure elevation	2.8 arcsec/(deg/s ²)	2.1 arcsec/(deg/s ²)
Lowest eigenfrequencies	5.57 Hz	6.8 Hz

- [9] A. G. Davenport, "The Application of Statistical Concepts to the Wind Loading of Structures", *Proc. of the Institute of Civil Engineers*, paper no. 6480, 1961, pp. 449-472.

APPENDIX I

MATHEMATICAL TREATMENT OF ACCELEROMETER SIGNALS

The mathematical treatment of the accelerometer data as covered in sections II and IV is elaborated in this appendix. Accelerometer measurements yield the acceleration as a function of time, as measured at the location of the accelerometer with the direction along the sensitive axis of the accelerometer.

In order to obtain a displacement signal from the measured accelerations, the signal needs to be integrated twice, since the acceleration $A(t)$ is by definition the second time t derivative of the displacement or position $X(t)$:

$$A(t) = \frac{d^2 X(t)}{dt^2} \quad (32)$$

Thus, for a given acceleration time series, the displacement becomes:

$$X(t) = \int \int A(t) d^2 t \quad (33)$$

where two integration constants need to be used. The integration constants are chosen in a way to minimise the mean and the slope of $X(t)$.

Many of the results in this paper are presented in the form of power spectra. The power spectrum of a time series $A(t)$ with n samples is defined by Equation 1, repeated here:

$$\hat{A}(\nu) = \frac{|FFT(A(t))|^2}{n^2} \quad (34)$$

where FFT is the fast Fourier transform. The normalisation with n^2 gives the power spectrum the property that the sum of all terms of $\hat{A}(\nu)$ equals the variance of the time series $A(t)$.

The power spectrum of a doubly integrated acceleration time series becomes thus:

$$\hat{X}(\nu) = \frac{|FFT(\int \int A(t) d^2 t)|^2}{n^2} \quad (35)$$

Consider now the special case where $X(t) = \sin 2\pi\nu_0 t$, a harmonic motion with frequency ν_0 . The second time derivative of $X(t)$ then becomes:

$$\begin{aligned} A(t) &= \frac{d^2 \sin 2\pi\nu_0 t}{dt^2} \\ &= -(2\pi\nu_0)^2 \sin 2\pi\nu_0 t \\ &= -(2\pi\nu_0)^2 X(t) \end{aligned} \quad (36)$$

which is equal to the time series $X(t)$ times a factor $-(2\pi\nu_0)^2$.

When the power spectrum is taken on either side of the equation, it results in the following expression:

$$\begin{aligned} \hat{A}(\nu) &= \frac{|FFT(-(2\pi\nu_0)^2 X(t))|^2}{k^2} \\ &= (2\pi\nu_0)^4 \hat{X}(\nu) \end{aligned} \quad (37)$$

where $|(2\pi\nu_0)^2|^2$ can be taken outside the Fourier transform since it is not a function of t . The remaining term is exactly the power spectrum of $X(t)$. Division by $(2\pi\nu_0)^4$ on either side of the equation gives:

$$\hat{X}(\nu) = \frac{\hat{A}(\nu)}{(2\pi\nu_0)^4} \quad (38)$$

Since any function can be described as a sum of sine functions with different amplitude, phase, and frequency, the frequency ν_0 in $(2\pi\nu_0)^4$ can be replaced with ν , the coordinate in the frequency domain of the power spectrum.

All power spectral densities (PSDs) presented in this paper are the square root of the power spectrum defined above, thus the PSD of a timeseries of accelerations, including double integration to obtain displacement, is given by:

$$PSD(X(t)) = \sqrt{\hat{X}(\nu)} = \frac{\sqrt{\hat{A}(\nu)}}{(2\pi\nu)^2} = \frac{PSD(A(t))}{(2\pi\nu)^2} \quad (39)$$



Ralph C. Snel received his M.Sc. degrees in astrophysics and experimental physics at the University of Utrecht in the Netherlands in 1991 and 1992, and his Ph.D. degree in astrophysics at Lund University in Sweden in 1998.

From observing stellar populations with the Hubble Space Telescope he turned his view downward and became involved as calibration scientist for the Earth atmosphere observing imaging spectrograph SCIAMACHY on the ESA Envisat satellite, at SRON Space Research in the Netherlands. From 2001 to 2003 he worked at Lund Observatory on development of an optical telescope in the 50 m class, and testing of the ALMA prototype antennas, which he continued under ESO and NRAO contracts in 2004. Recently, he joined SRON again for more Earth observation. In his spare time, he is often found at the anvil blacksmithing reconstructions of mediaeval arms and armour.



Jeffrey G. Mangum received the Ph.D. degree in astronomy from the University of Virginia in 1990.

Following a two-year residency as a postdoctoral researcher in the astronomy department at the University of Texas he joined the staff of the Submillimeter Telescope Observatory (SMTO) at the University of Arizona. In 1995 he joined the scientific staff at the National Radio Astronomy Observatory (NRAO) in Tucson, Arizona, and subsequently moved to the NRAO headquarters in Charlottesville, Virginia. His research interests include the astrophysics of star formation, the solar system, and external galaxies, the performance characterization of reflector antennas, and calibration of millimeter-wavelength astronomical measurements.



Jacob W. M. Baars received the M.Sc. and D.Sc. degrees in applied physics from the Technical University of Delft, the Netherlands in 1963 and 1970, respectively.

After working at the National Radio Astronomy Observatory in Green Bank, WV, he joined the Netherlands Foundation for Radio Astronomy in 1969. There he participated in the construction and was later head of the Westerbork Synthesis Radio Telescope. In 1975 he joined the Max-Planck-Institut für Radioastronomie in Bonn as head of the Division for Millimeter Technology. He was project Manager of the 30-m Millimeter Radio Telescope of IRAM in Spain and the Heinrich Hertz Telescope in Arizona. From 1997-99 he worked on the UMass-Mexico Large Millimeter Telescope. In 1999 he joined the European Southern Observatory, where he was involved in several aspects of the ALMA Project, lastly the evaluation of the prototype antennas. Since his retirement he consults in the area of large antennas and radio telescopes. His research interests are in the area of antenna theory and practice, in particular the performance calibration of large antennas with radio sources, and of atmospheric influences on observations at very high frequencies.